Magnetoelastic coupling associated with vacancy ordering and ferrimagnetism in natural pyrrhotite, Fe$_7$S$_8$

C R S Haines, G I Lampronti and M A Carpenter

Department of Earth Sciences, University of Cambridge, Downing Street, Cambridge CB2 3EQ, United Kingdom

E-mail: crsh2@cam.ac.uk

CrossMark

Abstract

Magnetoelastic coupling associated with the hexagonal—monoclinic transition in a natural sample of the mineral pyrrhotite, Fe$_7$S$_8$, has been analysed in terms of separate coupling of spontaneous strains with two discrete order parameters, q_v for Fe/vacancy ordering and q_m for magnetic ordering. Coupling of the two order parameters separately with strain gives rise to two terms for coupling between them, $\lambda q_m^2 q_v^2$ and $\lambda q_m^2 q_v^8$, and a pattern of evolution in which q_v varies continuously and q_m discontinuously through a single transition point. The transition is ferrimagnetic and ferroelastic but the relatively slow relaxation rate for Fe/vacancy ordering, in comparison with magnetic ordering, results in elastic and anelastic properties which are quite different from those observed in other ferroic or multiferroic materials with two instabilities. Instead of classical elastic softening, there is stiffening of the elastic constants which scales with q_m^2 and q_v^2. Instead of the normal pattern of acoustic loss associated with the mobility and subsequent freezing for ferroelastic twin walls, the loss is consistently low throughout the temperature range 300 K–875 K.

Keywords: pyrrhotite, Fe$_7$S$_8$, magnetoelastic coupling, vacancy ordering

(Some figures may appear in colour only in the online journal)

1. Introduction

A notable feature of the mineral pyrrhotite, Fe$_{1-x}$S, is that it displays wide variations in magnetic and thermodynamic properties over a narrow range of compositions corresponding to $0 > x > 0.125$ [1–6]. These have resulted in it having significance in contexts as disparate as palaeomagnetism on Earth [7] and Mars [8, 9], mineral exploration [10] and phase change magnetic memories [11]. Much of the diversity observed in natural and synthetic samples arises from the fact that small changes in iron content lead to a variety of superstructures

associated with ordering of vacancies on the cation site. The Néel temperature of ∼590 K [2] is nearly constant across the solid solution, but the symmetry of the magnetic ordering schemes which develop is controlled by the particular pattern of commensurate or incommensurate vacancy ordering at each composition. The expectation is that crystals will be ferrimagnetic if the vacancies are confined to alternate iron layers of the NiAs-type parent structure and antiferromagnetic if they occur equally in all layers. As a consequence, it is generally held that 'monoclinic' pyrrhotite will have a magnetic moment whereas 'hexagonal' pyrrhotite will not (but see Horng and Roberts 2018 [12]). Changes in the hard and soft directions for magnetic ordering as functions of composition and temperature lead to a further set of magnetic transitions below the primary Néel point, as summarised, for example, by Schwarz and Vaughan (1972) [2].

Table 1. Order parameters with symmetries of different irreducible representations for the changes in space group $P6_3/mmc \rightarrow C2'/c' \rightarrow P\bar{1}$, from Haines *et al* [19]. The basis vector is $(2,-2,0)$, $(2,2,0)$, $(-1,1,2)$ and the origin is $(0,1/2,0)$. *a* and *b* signify non-zero components of the multi-component order parameters. P1, P2, P4, C1 and C5 indicate the relevant order parameter directions, as given in the group theory program ISOTROPY [22].

	U1(1/2,0,1/4)	$m\Gamma_2^+$	$m\Gamma_4^+$	$m\Gamma_5^+$	$m\Gamma_6^+$
$P6_3/mmc$	(0,0,0,0,0,0)	(0)	(0)	(0,0)	(0,0)
$C2'/c'$	P4 (a,0,0,a,0,0)	P1 (a)	P1 (a)	P2 ($-a$,0.577a)	P1 (a,1.732a)
$P\bar{1}$	C5 (a,0,0,b,0,0)	P1 (a)	P1 (a)	C1 (a,b)	C1 (a,b)

The present study was initiated as part of a wider effort to characterise the strength and mechanisms of magnetoelastic phenomena in ferroic, multiferroic and superconducting phases through the influence of strain coupling on elastic and anelastic properties [13–17]. Pyrrhotites provide an interesting example of magnetoelastic behaviour in which magnetic ordering is coupled with vacancy ordering either directly or indirectly via common strains. The magnetic transitions are accompanied by small but measurable changes in lattice parameters, but the dynamics of strain coupling and relaxational processes are constrained by the timescale required for changes in Fe/vacancy order to occur, in comparison with the much shorter time scale of changes in local spin configurations. Experimental data of Herbert *et al* [18] for a sample with the 11C superstructure suggest that measurable changes in Fe/vacancy ordering can occur on a timescale of 10's to 1000's of seconds at ∼450–500 K and, by extrapolation, on a timescale of hours to 10's of hours at ∼350 K or years at ∼300 K. These results suggest that equilibrium might be maintained on a laboratory timescale between 600 K and ∼400 K, say, and on a geological time scale perhaps down to room temperature.

Symmetry relationships provide a framework of theory by which paramagnetic–antiferromagnetic/ferromagnetic transitions, Fe/vacancy ordering and Morin-type transitions across the whole range of pyrrhotite composition can be rationalised in terms of a well-defined set of macroscopic order parameters [19]. Here the focus is on coupling of ferrimagnetism and vacancy order with strain in the 4C monoclinic structure of Fe_7S_8 below ∼590 K. Because the symmetry changes are hexagonal → monoclinic → triclinic, this includes consideration of the development and properties of ferroelastic twin walls. Relevant aspects of symmetry changes associated with the hexagonal–monoclinic–triclinic sequence of phase transitions in Fe_7S_8 are summarised in section 2, below. A formal analysis of coupling between strain and the relevant driving order parameters, using lattice parameter data from the neutron powder diffraction study of Powell *et al* [21], is presented in section 3. Section 4 contains a description of the natural single crystal used for measurements of elastic and anelastic properties by resonant ultrasound spectroscopy (RUS). Implications of the strain and elastic properties are considered for the hexagonal ($P6_3/mmc$)–monoclinic ($C2'/c'$) transition in section 5. Magnetoelastic coupling associated with the Besnus

transition at ∼35 K in the same natural sample is described in an accompanying paper (see reference [20]).

2. Order parameters and symmetry

For Fe_7S_8, the space groups of the sequence of structures with falling temperatures which emerges from the analysis of Haines *et al* [19] is $P6_3/mmc$–$C2'/c'$–$P\bar{1}$, in agreement with the possibility of $P1$ or $P\bar{1}$ proposed by Wolfers *et al* [21] for the low temperature structure. The key order parameters and their non-zero components are listed in table 1. The $P6_3/mmc \rightarrow C2'/c'$ (4C structure) transition is driven by a combination of vacancy ordering, for which the order parameter has the symmetry of irreducible representation (irrep) U1(1/2,0,1/4), and magnetic ordering, for which the order parameter belongs to magnetic irrep $m\Gamma_5^+$. This combination gives secondary order parameters belonging to irreps $m\Gamma_2^+$, $m\Gamma_4^+$ and $m\Gamma_6^+$.

The direction P2 of $m\Gamma_5^+$ has non-zero components $(-a,0.577a)$ for the setting given in table 1. By itself, the equivalent $m\Gamma_5^+$ $(0,a)$ would give a magnetic structure with space group $Cm'c'm$, which would have moments aligned parallel to $[100]_H^*$ in ferromagnetic layers and antiferromagnetic alignments between layers. Subscript H is used here and below to signify indices given with respect to the parent hexagonal structure. In combination, $m\Gamma_4^+$ and $m\Gamma_5^+$ allow individual moments (and, hence, the net ferrimagnetic moment) to rotate within the a–c plane of the monoclinic structure, as reported by Powell *et al* (2004) [23]. It follows that the change in order parameter which would drive a transition from the $C2'/c'$ structure to $P\bar{1}$ is $m\Gamma_5^+$ $(-a,0.577a) \rightarrow m\Gamma_5^+$ (a,b). This allows rotation of the moments out of the a–c plane [19].

On its own, $m\Gamma_2^+$ would give a ferromagnetic structure with moments aligned parallel to $[001]_H^*$ while $m\Gamma_6^+$ with direction P1 $(a,0)$ would give a ferromagnetic structure with moments aligned parallel to $[100]_H^*$. Neither of these ferromagnetic ordering schemes has been observed in the monoclinic 4C ($C2'/c'$) structure, however, implying that the components of $m\Gamma_2^+$ and $m\Gamma_6^+$ are zero for reasons of thermodynamic stability.

3. Strain analysis

It is not possible to measure the values of order parameters directly and by far the most straightforward way of
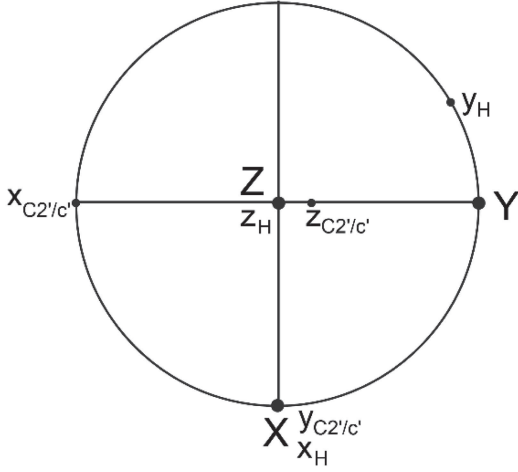
Figure 1. Setting of crystallographic axes of the parent hexagonal structure and product monoclinic structure, with respect to reference axes, X, Y, Z, as used to obtain the strain coupling terms in equation (1).

extracting their interdependence and variations with temperature are through measured variations of lattice parameters. If the order parameters are strictly zero in the high symmetry structure, it is necessary to choose reference states for calculation of the symmetry-adapted strains which also must be zero above the transition point. The reference system used here for analysis of spontaneous strains which couple with order parameters for vacancy ordering and magnetic ordering is shown in figure 1. In this setting, the basis vectors are $(-2,-4,0)$, $(2,0,0)$, $(1,2,2)$ with origin $(1/2,1/2,1/2)$ and the non-zero components of the U1$(1/2,0,1/4)$ order parameter are $(-0.707a, -0.707a, 0, 0, 0, 0.707a, -0.707a)$. For the purposes of producing a Landau expansion to describe the $P6_3/mmc-C2'/c'$ transition, the U1$(1/2,0,1/4)$ order

parameter can be represented as q_v and the non-zero component of the mΓ_5^+ order parameter as q_m. Coupling between the two order parameters and strain and between themselves then has the form (after Haines *et al* [19])

$$
\begin{aligned}
G =\ & \frac{1}{2}a_m\left(T - T_{cm}\right)q_m^2 + \frac{1}{4}b_m q_m^4 + \frac{1}{6}c_m q_m^6 + \frac{1}{2}a_v\left(T - T_{cv}\right)q_v^2 \\
& + \frac{1}{4}b_v q_v^4 + \frac{1}{6}c_v q_v^6 + \lambda_{em1}\left(e_1 + e_2\right)q_m^2 + \lambda_{em2}e_3 q_m^2 \\
& + \lambda_{em3}\left(e_1 - e_2\right)q_m^2 + \lambda_{em4}\left(3e_4^2 + e_5^2\right)q_m^2 + \lambda_{em5}e_6^2 q_m^2 \\
& + \lambda_{ev1}(e_1 + e_2)q_v^2 + \lambda_{ev2}e_3 q_v^2 + \lambda_{ev3}\left(e_1 - e_2\right)q_v^2 \\
& + \lambda_{ev4}\left((e_1 - e_2)^2 + 4e_6^2\right)q_v^2 + \lambda_{ev5}\left(e_4^2 + e_5^2\right)q_v^2 \\
& + \lambda_{ev6}\left(3e_4^2 + 5e_5^2\right)q_v^2 + \lambda_{ev7}e_4 q_v^4 + \lambda_{mv1}q_m^2 q_v^2 + \lambda_{mv2}q_m^2 q_v^8 \\
& + \frac{1}{4}\left(C_{11}^o + C_{12}^o\right)(e_1 + e_2)^2 + \frac{1}{4}\left(C_{11}^o - C_{12}^o\right)(e_1 - e_2)^2 \\
& + C_{13}^o(e_1 + e_2)e_3 + \frac{1}{2}C_{33}^o e_3^2 + \frac{1}{2}C_{44}^o\left(e_4^2 + e_5^2\right) + \frac{1}{2}C_{66}^o e_6^2.
\end{aligned}
\tag{1}
$$

T_{cm} and T_{cv} are critical temperatures for the magnetic and vacancy ordering transitions, respectively, a_v, a_m, b_v, etc, are standard Landau coefficients, e_i ($i = 1\text{–}6$) are components of the spontaneous strain tensor, λ's are coupling coefficients and C_{ik}^o (i, $k = 1\text{–}6$) are elastic constants of the hexagonal parent structure. The lowest order coupling between the two order parameters, either directly or indirectly via these strains, is biquadratic, $\lambda q_v^2 q_m^2$. Coupling between the monoclinic shear strain e_4 and q_v has the unusual form, $\lambda e_4 q_v^4$, whereas it couples with q_m as $\lambda e_4^2 q_m^2$. These two terms would lead to indirect coupling between q_v and q_m with the form $\lambda q_{m2}^2 q_v^8$.

The equilibrium condition, $\partial e/\partial G = 0$, gives strain/order parameter relationships as

$$
(e_1 + e_2) = \left(\frac{\left(2\lambda_{em2}C_{13}^o - 2\lambda_{em1}C_{33}^o\right)q_m^2 + \left(2\lambda_{ev2}C_{13}^o - 2\lambda_{ev1}C_{33}^o\right)q_v^2}{\left(C_{11}^o + C_{12}^o\right)C_{33}^o - 2C_{13}^{o\,2}}\right)
\tag{2}
$$

$$
e_3 = \left(\frac{\left(2\lambda_{em1}C_{13}^o - \lambda_{em2}\left(C_{11}^o + C_{12}^o\right)\right)q_m^2 + \left(2\lambda_{ev1}C_{13}^o - 2\lambda_{ev2}\left(C_{11}^o + C_{12}^o\right)\right)q_v^2}{\left(C_{11}^o + C_{12}^o\right)C_{33}^o - 2C_{13}^{o2}}\right)
\tag{3}
$$

$$
(e_1 - e_2) = -\left(\frac{2\lambda_{em3}q_m^2 + 2\lambda_{ev3}q_v^2}{4\lambda_{ev4}q_v^2 + \left(C_{11}^o - C_{12}^o\right)}\right) \approx -\left(\frac{2\lambda_{em3}q_m^2 + 2\lambda_{ev3}q_v^2}{\left(C_{11}^o - C_{12}^o\right)}\right) \text{ for } \left(C_{11}^o - C_{12}^o\right) \gg 4\lambda_{ev4}q_v^2
\tag{4}
$$

$$
e_4 = -\left(\frac{\lambda_{ev7}q_v^4}{6\lambda_{em3}q_m^2 + 2\lambda_{ev5}q_v^2 + 6\lambda_{ev6}q_v^2 + C_{44}^o}\right) \approx -\left(\frac{\lambda_{ev7}q_v^4}{C_{44}^o}\right) \text{ for } C_{44}^o \gg 6\lambda_{em3}q_m^2 + 2(\lambda_{ev5} + 3\lambda_{ev6})q_v^2.
\tag{5}
$$

Individual strains are determined from lattice parameters according to (eg see Carpenter and Salje [24])

$$
e_1 = ((b/2) - a_o)/a_o
\tag{6}
$$

$$
e_2 = \left(\left(a/2\sqrt{3}\right) - a_o\right)/a_o
\tag{7}
$$

$$
e_3 = ((c/4) - c_o)/c_o
\tag{8}
$$

$$
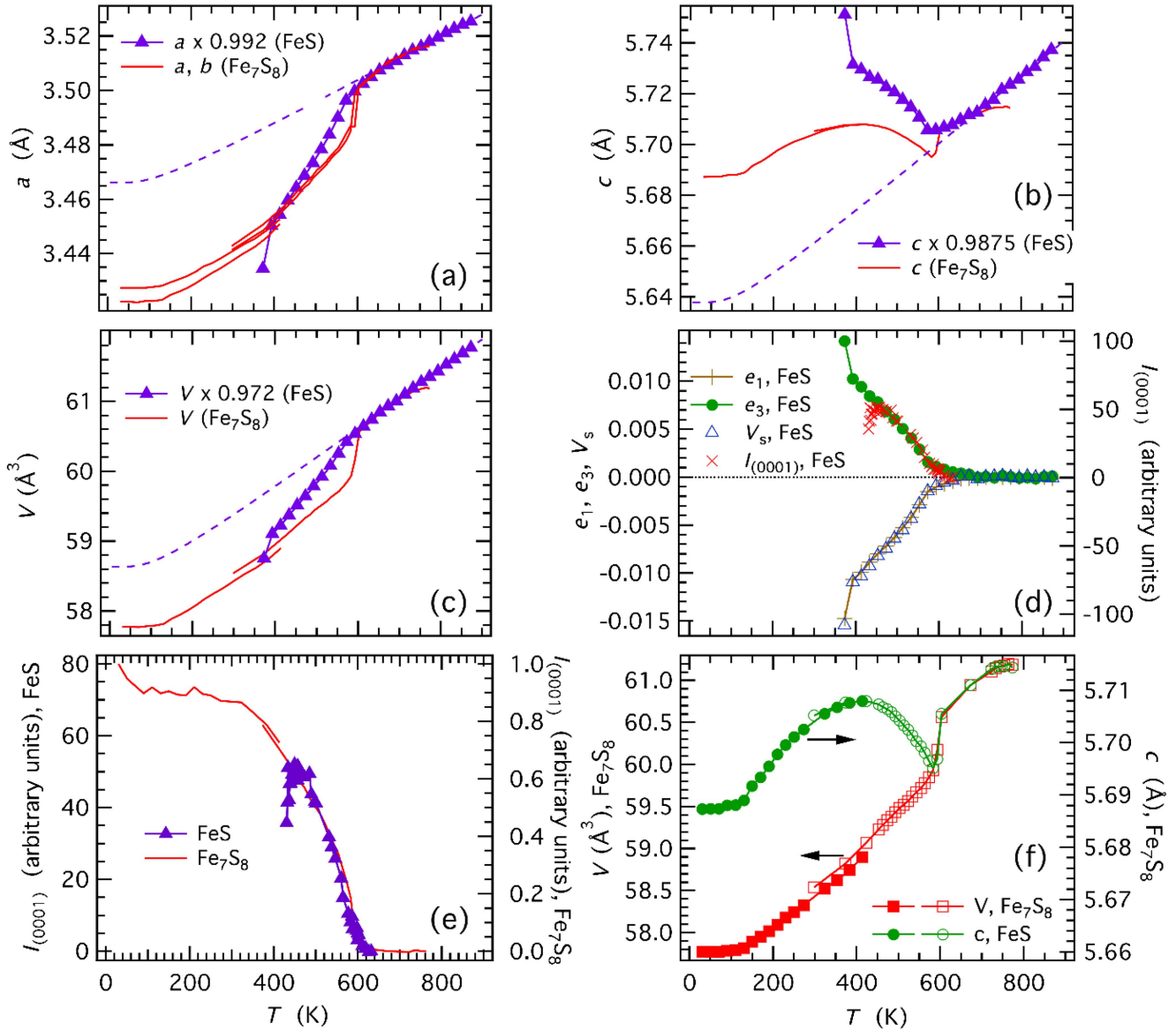V_s = ((V/16\sqrt{3}) - V_o)/V_o \approx (e_1 + e_2 + e_3)
\tag{9}
$$

Figure 2. (a)–(c) Lattice parameter data for troilite, FeS, from Tenailleau *et al* [25], shown as filled triangles, in comparison with those for the pseudohexagonal cell of Fe_7S_8 from Powell *et al* [23], shown as red lines. The FeS data have been scaled by factors given in the legends so that they overlap with the Fe_7S_8 data at temperatures above 600 K. Dashed lines represent reference parameter, a_o, for the FeS structure, as obtained by fitting the expression $a_o = a_1 + a_2\Theta_s \coth(\Theta_s/T)$, and similarly for c_o, V_o. The saturation temperature, Θ_s, was fixed at 150 K. In this sample, a second magnetic transition occurred at $\sim$390 K. (d) Spontaneous strains for FeS, calculated from the data in (a)–(c), compared with the intensity of a superlattice reflection, $I_{(0001)}$, from neutron powder diffraction of Andresen *et al* [31]. The second transition occurred at $\sim$440 K in the sample of Andresen *et al* [31]. The right axis is scaled to demonstrate $I_{(1000)}$ ($\propto q_m^2$) $\propto e_3$. (e) Comparison of $I_{(1000)}$ for the 4C structure of Fe_7S_8 from Powell *et al* [23] with data for FeS from Andresen *et al* [31], showing that magnetic ordering has essentially the same temperature dependence in each phase. (f) Comparison of V and c parameters for Fe_7S_8, scaled so that they overlap at $T \geqslant 600$ K. Open and filled symbols represent data from two different instruments in the original work of Powell *et al* [23]. Data for c show the same form of steep change at $\sim$600 K as seen in the data for V, but the trend is then immediately reversed.

$$e_4 = \frac{c/4}{c_o}\cos\beta^* \approx \cos\beta^* \qquad (10)$$

$$e_5 = e_6 = 0. \qquad (11)$$

Here a, b, c, β^* and V refer to the $F2/d$ cell of the monoclinic structure, rather than the $C2/c$ cell. a_o, c_o and V_o are reference parameters of the parent hexagonal structure, extrapolated into the stability field of the monoclinic structure.

Separation into strain contributions due to coupling with q_v and q_m is made possible by comparison of the lattice

parameter data of Powell *et al* [23] for Fe_7S_8 with data of Tenailleau *et al* [25] for a natural sample of FeS, troilite, which has antiferromagnetic ordering without vacancy ordering. The change in symmetry expected on the basis of group theory for FeS is $P6_3/mmc \rightarrow Pnma$ (moments parallel and antiparallel to $[010]_H$ in alternate layers) or $Pnm'a'$ (moments parallel and antiparallel to $[100]_H^*$ in alternate layers) [19]. Tenailleau *et al* [25] were able to fit their neutron powder diffraction patterns with hexagonal lattice parameters down to at least $\sim$400 K,
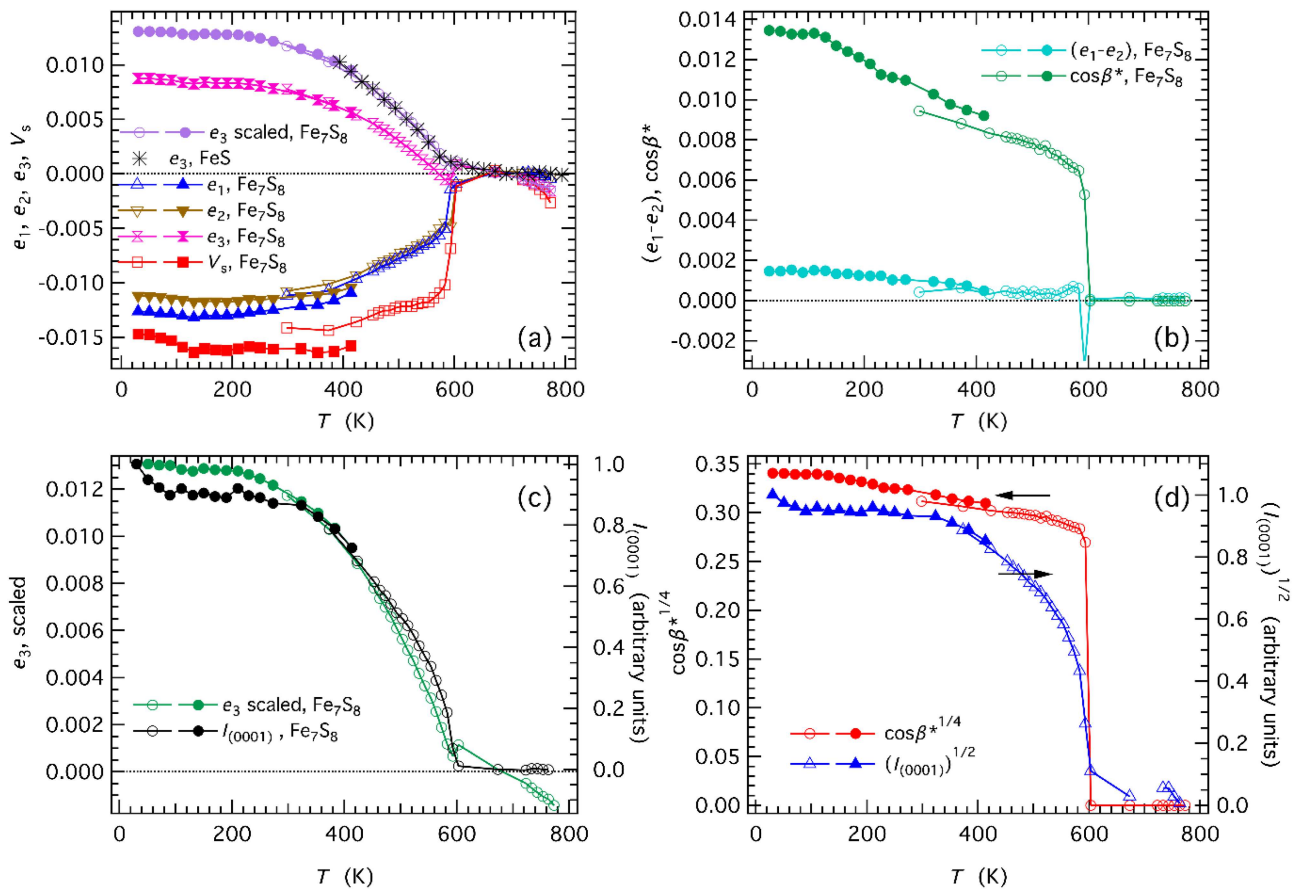
Figure 3. Strain analysis based on neutron powder diffraction data of Powell *et al* [23] for a synthetic sample of 4C pyrrhotite and baseline parameters from FeS. (a) Non symmetry-breaking strains, e_1, e_2, e_3, V_s, all show a step-like reduction between 603 and 593 K, followed by smooth variations with falling temperature. 'e_3 scaled' is the value of e_3 after subtraction of a component scaled with respect to the average variations of e_1 and e_2 in proportion to the step at $\sim$600 K; it overlaps with data for e_3 of FeS which are also shown. (b) Symmetry-breaking shear strains, $(e_1 - e_2)$, $\cos \beta^*$ ($\approx e_4$). $(e_1 - e_2)$ values remain low at all temperatures, while $\cos \beta^*$ shows a steep increase at $\sim$600 K, consistent with first order character for the hexagonal–monoclinic transition. The single negative value of $(e_1 - e_2)$ at 593 K is presumed to be an artefact. (c) Comparison of $I_{(0001)}$ with the variations of 'e_3 scaled', showing that part of the e_3 strain has a similar variation with q_m^2 to that of e_3 in FeS. (d) Variations with temperature of $(I_{(0001)})^{1/2}$, representing q_m, and $\cos \beta^{*1/4}$, representing q_v. $\cos \beta^{*1/4}$ has a steep discontinuity between 603 and 593 K, while $(I_{(0001)})^{1/2}$ varies continuously and has a tail due to short range ordering above 600 K.

indicating that the distortion from hexagonal geometry was small, ie that coupling of q_m^2 with the symmetry-breaking shear strain $(e_1 - e_2)$ was weak. The two sets of lattice parameters are reproduced in figure 2, with the data for FeS scaled so that they overlap with data for the hexagonal cell of Fe_7S_8 above 600 K. It is worth noting that this scaling produces close overlap for the two samples when $q_v = q_m = 0$, implying that their evolution ahead of the phase transitions is almost identical, i.e. including precursor effects due to fluctuations.

Also shown in figure 2 are baselines of the form $a_o = a_1 + a_2 \Theta_s \coth(\Theta_s/T)$ [26–30] which were obtained by fitting to values for a, c and V of FeS in the interval 693–873 K. The saturation temperature, Θ_s, was fixed at 150 K in order to provide a semi-quantitative representation of the physically correct form of variation as $T \rightarrow 0$ K. The a parameter of FeS decreases through T_N while c increases, giving the continuous variations of linear strains e_1 and e_3 shown in figure 2(d). Although not required by symmetry, $|e_3|$ is almost equal to $|e_1|$. Overall, there is a negative volume strain, V_s. The intensity

of the (0001) magnetic superlattice reflection, $I_{(0001)}$, in powder neutron diffraction is expected to scale with the square of the magnetic order parameter, and data of Andresen *et al* [31] show that it also scales with e_3 (figure 2(e)). This is consistent with e_3 ($\propto e_1 \propto V_s$) $\propto q_m^2$. Fe_7S_8 differs from FeS by having additional negative and apparently discontinuous reductions in a, c and V at the transition point (figures 1(a)–(c)). Figure 2(f) highlights this aspect of variations of V and c which have been scaled to show that the increase in c below the transition point is preceded by the same form of reduction, though it is smaller in magnitude.

Variations of non-symmetry-breaking strains, e_1, e_2, e_3, V_s, and symmetry-breaking shear strains $(e_1 - e_2)$ and $\cos \beta^*$ for Fe_7S_8, using the lattice parameters of Powell *et al* [23] and baselines from FeS, are shown in figures 3(a) and (b), respectively. Each of e_1, e_2, e_3 and V_s ($\approx e_1 + e_2 + e_3$) display the same steep and apparently discontinuous reduction between 603 and 583 K, followed by smooth variations with further lowering of temperature. $(e_1 - e_2)$ remains small at all temperatures, consistent with the weak coupling already inferred
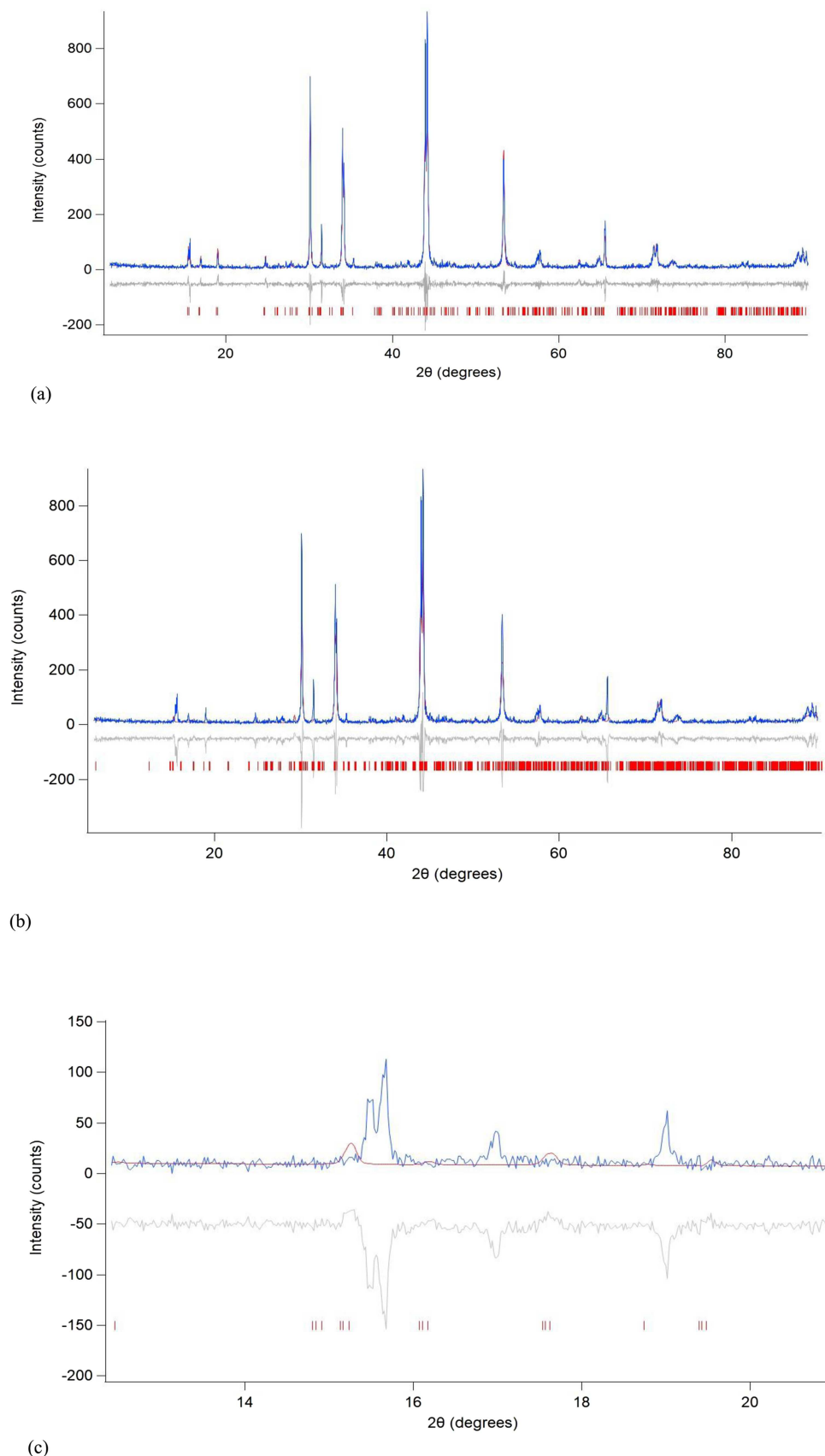
Figure 4. Comparison of observed and calculated intensities from Rietveld refinements of x-ray powder diffraction data. (a) Result of refinement based on the 4C structure of Powell *et al* [23]. (b) Result of refinement based on the 5C structure of Liles *et al* [34]. (c) Expanded view of a section of (b), showing that the 5C structure does not fit the tell-tale peaks at low diffraction angles.

Table 2. Unit cell dimensions from Rietveld refinements using the model of Powell *et al* [23] for the 4C pyrrhotite structure and the model of Liles and de Villiers [34] for the 5C structure.

	a (Å)	b (Å)	c (Å)	β (°)	V (Å^3)
4C ($C2/c$)	11.9137(7)	6.8671(5)	12.9113(7)	118.01(4)	932.5(1)
5C ($P2_1$)	6.907(1)	28.389(4)	6.8578(9)	120.07(1)°	1163.8(3)

for FeS. Cos $\beta^* \approx e_4$ has a steep increase below 603 K and reaches a maximum value of $\sim 1.4\%$.

Recovery of c following the initial steep reduction can be separated out as a strain parameter if the overall volume change is assumed to contain a component in the c-direction which continues to scale with a and b in the same way down to lower temperatures. A strain parameter 'e_3 scaled' has therefore been obtained by first scaling the average values of e_1 and e_2 so that they overlap with e_3 from 773 down to 593 K, and then subtracting this scaled average from the observed values of e_3. Figure 3(a) shows that 'e_3 scaled' is indistinguishable from e_3 for FeS, while figure 3(c) shows that it also varies in proportion to $I_{(0001)}$ from figure 4 of Powell *et al* [23]. These relationships indicate, firstly, that magnetic ordering in Fe_7S_8 follows the same temperature dependence as in FeS and, secondly, that the strength of coupling of the magnetic order parameter with strain in the crystallographic c-direction is independent of composition.

Powell *et al* [23] reported a hysteresis of ~ 5 K between the $P6_3/mmc$–$C2'/c'$ transition temperature measured during heating and cooling of their synthetic sample, while Herbert *et al* [18] have reported a hysteresis of 2 K for a natural sample. This is consistent with the first order character for the transition they inferred from the steep changes in lattice parameters between 603 and 593 K. However, there is a marked contrast between the evolution of the two order parameters, as highlighted in figure 3(d), which shows $(I_{(0001)})^{1/2}$ and, hence q_m, varying continuously through the transition point, while $\cos \beta^{*1/4}$, representing q_v, shows the first order discontinuity at ~ 600 K. Direct measurement of magnetisation also appears to show a continuous variation of the saturation remanence [32].

4. Experimental methods and results

4.1. Sample characterisation

The natural pyrrhotite sample selected for detailed investigation was a shiny, bronze coloured, cm-sized cluster of single crystals with well-developed crystal faces. It came from the mineral collection of the South Australia Museum and had originated from a mine in Mexico.

One large single crystal had faces consistent with a hexagonal growth habit. Indexing of the faces as (001) and (100) was confirmed by x-ray diffraction. Samples with faces cut perpendicular to [001], [100] and [$\bar{1}20$], as defined with respect to hexagonal axes, were prepared from this using a fine annular saw. The sample used for high temperature RUS measurements was nearly in the shape of a rectangular parallelepiped with two pairs of parallel faces 1.7 mm and 1.5 mm apart and a

third pair of non-parallel faces separated by between 1 mm and 1.5 mm. A small piece of the original single crystal with oriented faces was mounted and polished for chemical analysis using a Cameca SX100 electron microprobe in the Department of Earth Sciences, University of Cambridge (instrumental conditions: 20 keV, 10 nA, 1 μm beam diameter). With respect to eight sulphur atoms, the average of eight analyses gave the number of Fe atoms as 7.00 ± 0.06. Co, Cu, Mn, Ni and Zn were measured for, but all were below the detection limit on all of the eight analysis spots.

4.2. X-ray diffraction

An x-ray powder diffraction pattern was obtained from a ground up piece of the original pyrrhotite sample, using Bragg–Brentano geometry on a D8 Bruker diffractometer equipped with a primary Ge monochromator, Cu Kα_1 radiation and a Sol-X solid state detector. Conditions for the data collection were: 5–70° 2θ, 0.02° step size, 12 s/step, 0.2 mm divergence slit, 0.2 mm receiving slit, rotating sample. Rietveld refinements were performed with software Topas v6. [33], starting with 4C [23] and 5C [34] structures of Fe_7S_8 retrieved from the Inorganic Crystal Structure Database [35]. NIST standard LaB6 660b was used to model the instrumental parameters, following a fundamental parameters approach [36]. A shifted Chebyshev function with six parameters and pseudo-Voigt TCHZ function were used to model the background and the peak shape respectively. Figure 4(a) shows the match of the refined 4C structure, based on the model of Powell *et al* [23], with the observed diffraction pattern ($C2/c$, $r_{wp} = 26.98$, $r_{exp} = 21.2$, $\chi^2 = 1.27$). Most natural samples contain a mix of 4C and 5C phases. In order to check whether this was the case for the sample used in this study we also performed a refinement on the basis of a 5C structure. Figure 4(b) shows the same comparison between observations and a refinement starting from the 5C structure given by Liles and de Villiers [34]. (P2$_1$, $r_{wp} = 38.60$, $r_{exp} = 21.2$, $\chi^2 = 1.82$). Lattice parameters from both refinements are given in table 2.

4C and 5C superstructures share the same NiAs substructure so that most of the diffraction peaks, especially at higher angles, will be closely similar. The low angle peaks correspond to large d-spacings and provide the most important means of distinguishing between different superstructures. Refinement on the basis of the 5C structure produces a worse fit to the data, statistically, and does not match the low angle peaks (figure 4(c)). Refinement on the basis that both structures were present increased the number of fitting parameters but did not lead to a significant improvement in the fit ($\chi^2 = 1.26$) in comparison with the result for the 4C structure alone ($\chi^2 = 1.27$).
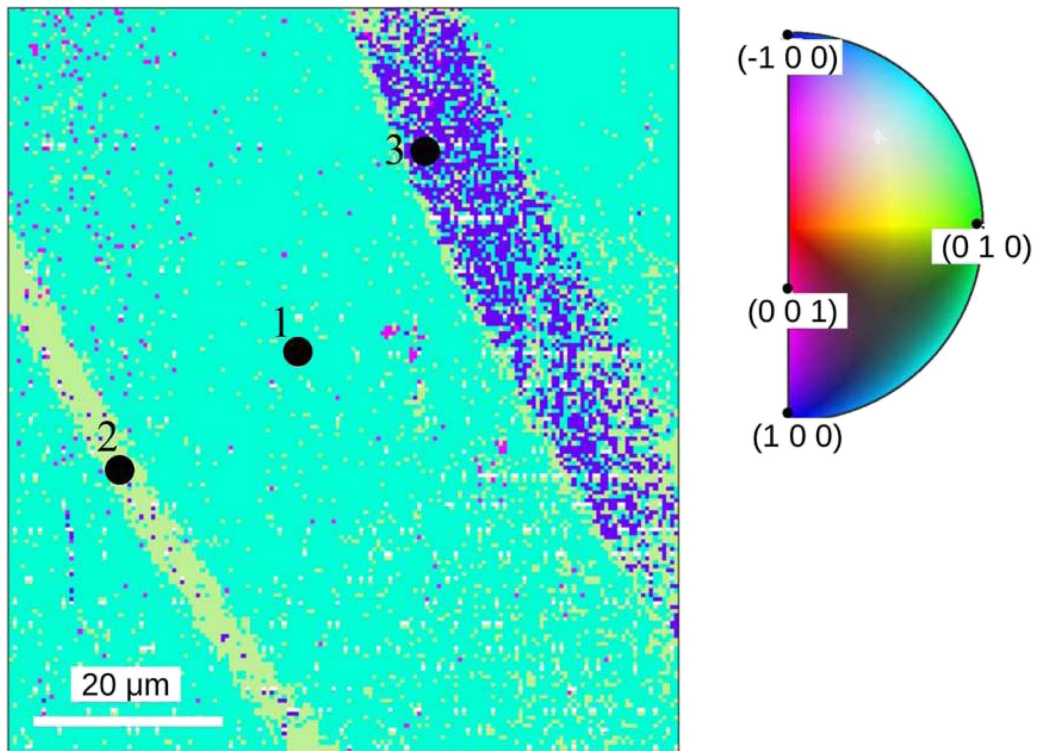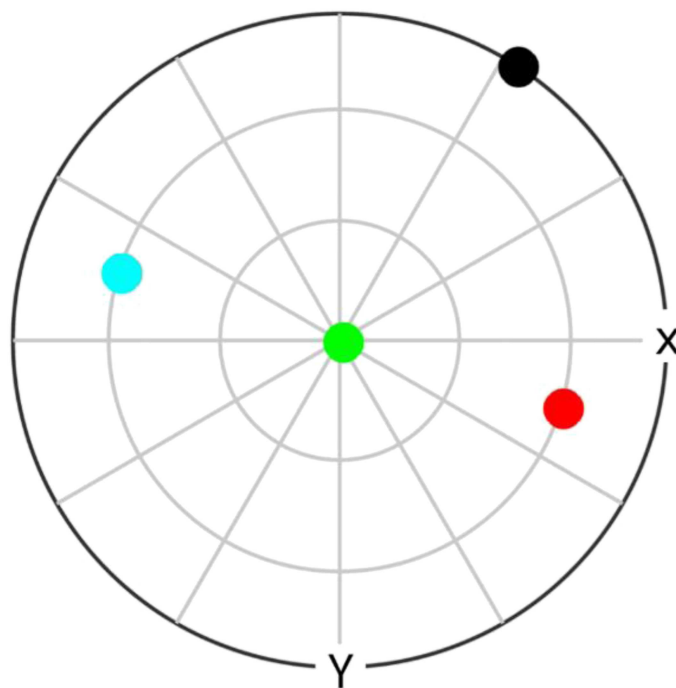
Figure 5. (a) Inverse pole figure map along the hexagonal parent unit cell *c* axis direction. Numbered black circles show the approximate regions used for the determination of the orientation of the three individuals given in figure (b). (b) Pole figure plot showing the [010] direction of each colour of the inverse pole figure map (red corresponding to region 1, blue, region 2, and green, region 3, markers), representing the three individuals of the pyrrhotite 4C twinned crystal. The black marker shows the orientation of the hexagonal parent unit cell *c*-axis direction.

It has therefore been concluded that any 5C pyrrhotite in the sample was below the level of detection.

4.3. Microstructure

The configuration of ferroelastic twins due to a change in point group symmetry $6/mmm \rightarrow 2/m$ is accompanied by shear strain which, in tensor form for one orientation variant, can be expressed as [37]

$$S = \begin{bmatrix} p & 0 & q \\ 0 & -p & 0 \\ 0 & 0 & 0 \end{bmatrix}.$$

The transition will produce six twin orientations with W and W' twin walls in three pairs, parallel to $(1, \sqrt{3}, 0)$ and $(-3p/2, \sqrt{3}p/2, -q)$, parallel to (100) and (001), and parallel to $(-1, \sqrt{3}, 0)$ and $(3p/2, \sqrt{3}p/2, q)$, using Miller indices defined with respect to orthogonal reference axes [37]. From the lattice parameter data shown in figure 2, values of $|p|$ and $|q|$ are $\leqslant \sim 1\%$. This means that most of the twin walls arising from vacancy ordering will be aligned nearly parallel to the $[001]^*$, though there will also be one set aligned parallel to (001). Because of the increase in the repeat distance parallel to c by a factor of four, there will also be antiphase domains with boundaries that involve translational errors of the ordered structure [38]. Segments of the boundaries between the antiphase domains which are oriented parallel to (001) can be non-conservative in the sense of having a local change in Fe:S ratio [38].

Electron back-scattered diffraction (EBSD) observations on a freshly cleaved surface of a pieces of the original sample used in the present study confirmed the presence of ferroelastic twin walls, as shown in figure 5(a). In this image, twins with three distinct orientations can be observed. The orientations are as expected for a hexagonal system, i.e. they are separated by 60 degrees in a pole plot in the reference axes of the low symmetry monoclinic phase (figure 5(b)). The twin individuals are separated by straight walls and have widths of a few micrometres up to several tens of micrometres. The EBSD data have a resolution of 0.4 μm and were collected on an FEI Quanta 650FEG SEM equipped with a Bruker e- Flash HR EBSD detector, operating at 20 kV and beam spot size 5.8 (beam current ∼10 nA). The detector resolution was 320×240 pixels, while working distance and sample to detector distance were 26.4 mm and 13.0 mm respectively. The data collection and indexing was perfomed with Bruker QUANTAX CrystaAlign software. Data were analysed using MTEX V5.0.3 [39], a freeware toolset for the commercial software package MATLAB. The misorientation angle precision was estimated to be ∼0.2 degrees using a linear fit of a misorientation profile from the dataset [40].

There must also be six possible directions for the ferrimagnetic moment in the monoclinic structure. In the accompanying paper [20], the orientation of the net magnetic moment is used to confirm the presence of multiple magnetic twins, with a net moment that lies in the (001) plane. In order to visualise the domain structure, we used the Bitter technique, in which a thin layer of a magnetic colloidal suspension, or ferrofluid, is applied to the surface and the magnetic
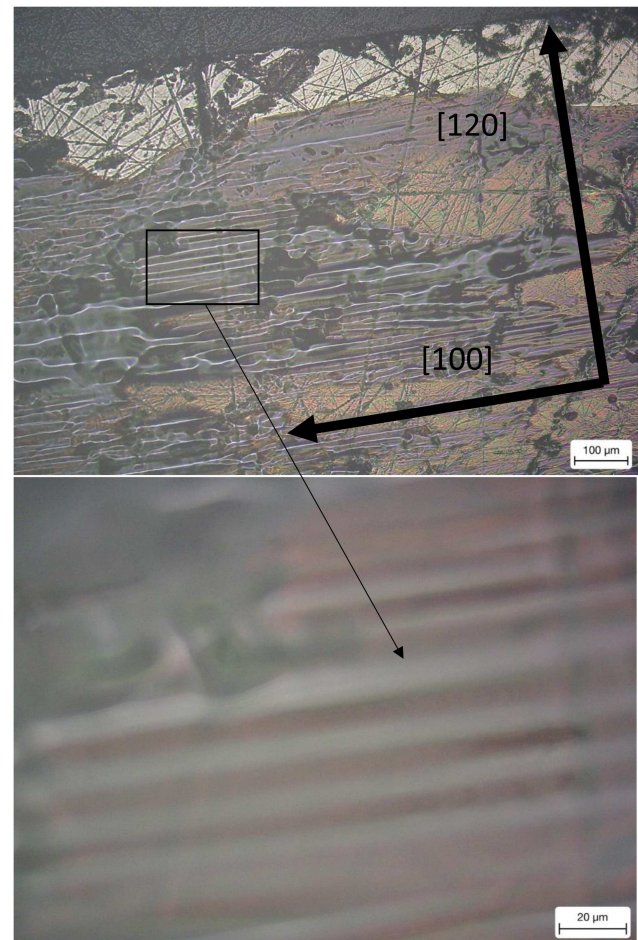

Figure 6. (a) Bitter pattern of a large area of the polished face of an oriented crystal. The vectors normal to two set of planes show the crystal directions. The (001) plane is in the plane of the page. (b) Close up of a selected area showing regularly spaced parallel domain walls.

particles are attracted to the high field gradients present at the domain walls [41]. Bitter patterns from the polished face of the sample used in the electron microprobe analysis are shown in figures 6(a) and (b). Previous reports of magnetic domain configurations in natural pyrrhotite grains using the Bitter technique and the Magneto-optical Kerr effect have shown a characteristic pattern of lamellar 180° domains on a scale of ∼2–30 μm [42–46]. Although not specified, the polarity of these domains is presumably parallel and antiparallel to the orientation of the individual moments determined by neutron diffraction, with domain walls close to (001) at room temperature.

4.4. Resonant ultrasound spectroscopy

RUS involves excitation of acoustic resonances of a mm-sized sample and measurement of the resulting spectra [47–51]. Individual resonance modes are dominated by shearing motions so that the results for their frequency, f, and peak width at half height, Δf, provide information predominantly relating to shear elastic constants. The elastic constants scale with f^2, and acoustic loss is expressed in terms of the inverse
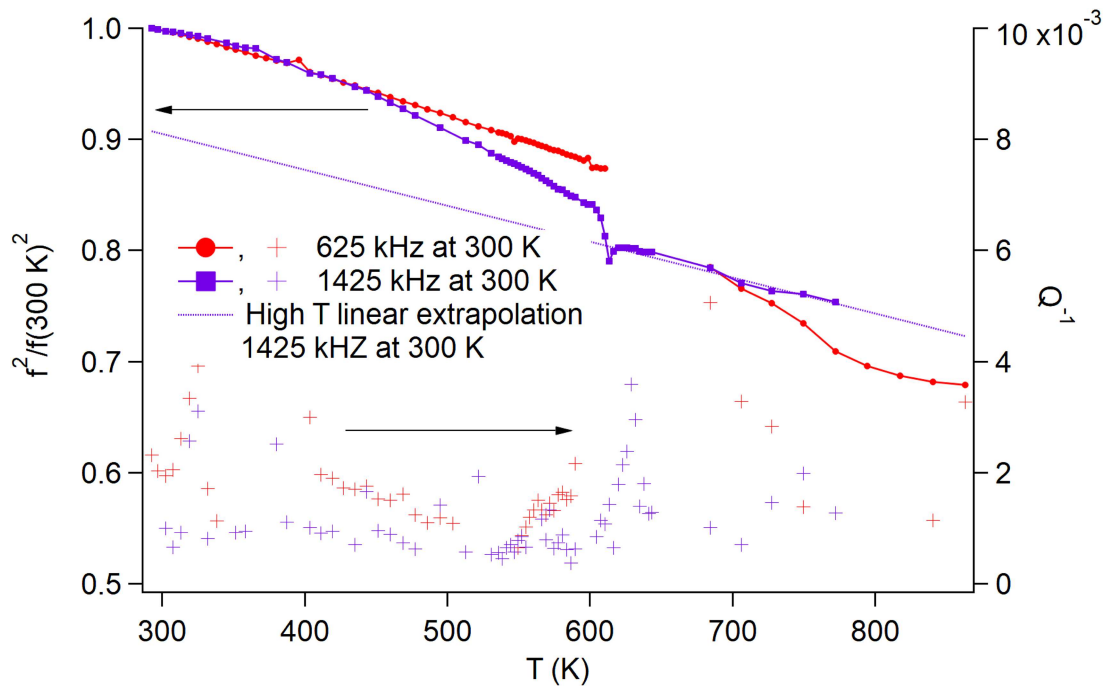
Figure 7. Variations of f^2 and Q^{-1} for two resonances in RUS spectra collected during heating from room temperature to 875 K.

mechanical quality factor, Q^{-1}, which is usually taken to be $\Delta f/f$. In the experimental set up used in the present study [54], the parallelepiped sample was held lightly across its corners between alumina buffer rods inserted into a horizontal tube furnace. Temperature is measured using a thermocouple located within a few mm of the sample and a final calibration is made based on the transition temperature of quartz.

Spectra were collected in an automated heating sequence from room temperature up to 875 K, with a settle time of 20 min to allow thermal equilibration at each set point. Variations of f^2 and Q^{-1} extracted from the primary spectra are shown in figure 7. Some oxidation of the sample occurred at the highest temperatures, so that it was not possible to follow the reverse sequence during cooling. f^2 of a resonance peak with frequency near 625 kHz at room temperature decreased smoothly (elastic softening) with increasing temperature. The peak broadened and disappeared altogether in the interval 611–684 K, signifying stronger attenuation. Relatively sharp peaks ($Q^{-1} \sim 5 \times 10^{-3}$) reappeared in the primary spectra at 684 K and above, with a net elastic softening of $\sim$8% across the transition point. Data for a resonance peak with frequency near 1420 kHz at room temperature allowed the pattern of f^2 variations through the transition temperature to be more clearly defined. There is a minimum in f^2 at 614 K, with softening by $\sim$5% between temperatures below and above this. As defined with respect to the parent $P6_3/mmc$ structure, represented by extrapolation of a straight line to data above 684 K (dashed line in figure 7), the $C2'/c'$ structure stiffens abruptly at the transition point and then more gradually with falling temperature. The overall pattern for the change in f^2 is closely similar to the form of variation shown by the strains V_s (figure 3(a)) and $\cos \beta^*$ (figure 3(b)). The most striking thing about the evolution of Q^{-1} is that it is rather low across the whole temperature range. There may be a small increase in Q^{-1} in the vicinity of

the phase transition, but it is never larger than fractions of one percent.

5. Discussion

The Néel temperature for FeS, troilite, is $\sim$590 K (e.g. reference [52] and references therein), and the temperature of the onset of magnetic ordering is essentially the same across the $Fe_{1-x}S$ solid solution to at least Fe_7S_8, irrespective of whether or not it is accompanied by vacancy ordering [5, 12, 53]. Based on the neutron diffraction data of Powell *et al* [23], the onset temperatures for magnetic ordering and vacancy ordering are indistinguishable, though the two order parameters have markedly different trajectories. The magnetic ordering transition is essentially the same as occurs in FeS with respect to transition temperature, the temperature dependence of q_m and the strength of coupling between q_m and strain. Strains that reflect the variation of q_v have a discontinuity at the transition point while q_m varies continuously through it (figure 3(d)). The overall behaviour is of a long-range magnetic ordering transition accompanied by significant secondary vacancy ordering that gives the first order character. Superposition of the two contributions in this way is consistent also with the form of the excess heat capacity shown by Grønvold and Stølen [53] which, for Fe_7S_8 (their figure 6), looks like the excess heat capacity for FeS (their figure 2) combined with an additional latent heat.

Strictly speaking, conventional Landau potentials refer to phase transitions at the displacive limit and will not reproduce the temperature dependence of the two order parameters in detail for order/disorder processes. However, an expansion of the form of equation (1) is expected to at least give the correct overall form for the observed variation of q_m with respect to
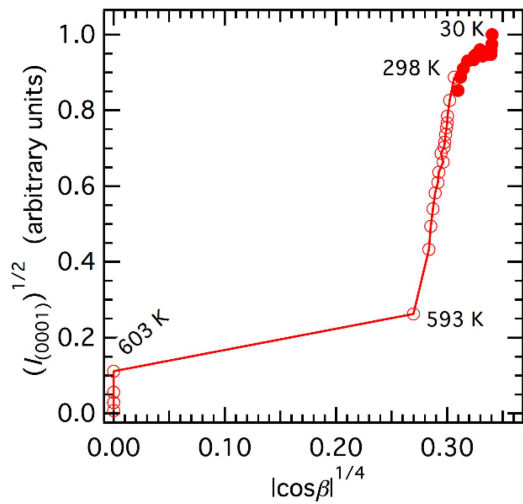
Figure 8. Variation of $(I_{(0001)})^{1/2}$, representing the variation of q_m, with respect to $\cos \beta^{*1/4}$, representing the variation of q_v. The initial increase in $(I_{(0001)})^{1/2}$ at $\cos \beta^{*1/4} = 0$ is due to short range ordering above the transition point. This is followed by an apparently discontinuous increase in $\cos \beta^{*1/4}$, followed by a smooth variation of both parameters down to 30 K. Between 593 and $\sim$300 K the variation is linear.

q_v, as represented by the variations of $(I_{(0001)})^{1/2}$ and $\cos \beta^{*1/4}$ in figure 8. The lowest order term for coupling between q_m and q_v is biquadratic and is most likely to be the result of a common strain mechanism. Coupling would be favourable via $(e_1 + e_2)$ since both order parameters induce negative values for this strain, but unfavourable via e_3 because q_m causes the *c*-dimension to increase and q_v causes it to decrease. The volume strain is negative in both cases, however, so that the coupling is likely to be favourable overall.

Generic models of biquadratic order parameter coupling based on two 246 potentials were treated in some detail by Salje and Devarajan [54]. If the coupling is weak, two successive transitions are expected unless the transition temperatures are coincident. Here we propose that there is one transition temperature set by the magnetic ordering. The vacancy ordering then takes place due to coupling with the magnetism through common strain. It is certainly not the case that q_m varies independently of q_v in Fe_9S_{10} because abrupt changes in temperature produce relatively slow changes in moment as the degree of Fe/vacancy order re-equilibrates [55]. Analogous kinetic evidence of coupling, also in Fe_9S_{10}, has also been reported by Marusak and Mulay [56] and Herbert *et al* [18].

The models of Salje and Devarajan [54] for strong coupling included only situations where the coefficient of the fourth order term was positive for both order parameters and did not produce any pattern of variations resembling that shown in figure 8 for the $C2'/c'$ structure of Fe_7S_8. Bilinear coupling between two order parameters, i.e. with the form $\lambda q_1 q_2$, and linear-quadratic coupling, i.e. of the form $\lambda q_1 q_2^2$, can result in two separate transition temperatures being renormalised to one [54, 57], but neither are allowed in this case. Instead, there is an unusual higher order coupling with the form $\lambda q_m^2 q_v^8$ that arises as a consequence of the coupling terms $\lambda e_4 q_v^4$ and $\lambda e_4^2 q_m^2$ in

equation (1). The implications of this unusual term have not been explored but, given that the magnetic ordering is the same as in FeS (without vacancy ordering), the outcome represented in figure 8 is presumably that symmetry breaking is driven by the magnetic instability and that coupling of the strain with the magnetic order parameter generates a field which induces vacancy ordering.

The normal expectation for changes in elastic constants associated with phase transitions is that softening will occur in the low symmetry phase due to coupling of strains with the driving order parameter [24, 58, 59]. The paramagnetic–antiferromagnetic transition in CoF_2 provides an example of this classical mechanism arising from coupling of the form $\lambda e q^2$ [60]. In Fe_7S_8, elastic stiffening is observed instead of softening (figure 7), but this is readily understandable in terms of the slow timescale of the relaxation of the order parameter with respect to the timescale of the applied stress. Changes in vacancy order give rise to a large shear strain, e_4, but applying a stress at a frequency of $\sim$1 MHz, does not allow time for q_v to relax. Instead, the elastic constants depend primarily on the second derivative of the excess free energy with respect to strain, $\delta^2 G/\delta e^2$, and therefore scale with combinations of q_m^2 and q_v^2 due to terms of the form $\lambda e^2 q^2$. For example, C_{44} will soften or stiffen according to $C_{44}^o + 6\lambda_{em3}q_m^2 + 2(\lambda_{ev5} + 3\lambda_{ev6})q_v^2$, and similarly for the other elastic constants. The step in f^2 at $\sim$600 K and further non-linear increases with falling temperature are thus expected to follow the variation of V_s, which scales with q_m^2 and q_v^2, as appears to be the case. Stiffening rather than softening reflects positive values of λ in each of the $\lambda e^2 q^2$ terms.

When measured at RUS frequencies, the mobility of ferroelastic twin walls in perovskites through some interval below a ferroelastic transition temperature and above the pinning/freezing temperature of the walls gives rise to a characteristic pattern of high attenuation [61]. The $P6_3/mmc$–$C2'/c'$ transition in Fe_7S_8 is, in principle, ferroelastic but switching of the resulting ferroelastic domains in response to an applied stress requires local reordering of the vacancies at the twin walls and will be slower by many orders of magnitude than switching of domains in materials where the ferroelasticity arises from a displacive phase transition. Even close to the transition temperature, it seems unlikely that this mechanism for acoustic loss will operate and the observed high attenuation is more likely to be intrinsic. Given that there is significant coupling between strain and the magnetic order parameter at a macroscopic scale, one source of the high loss would be changes in local spin state in response to the dynamic stress within a mechanical resonance of the sample. The degree of loss is highest close to and immediately below the transition point and, instead of there being evidence Debye peak in Q^{-1} to mark a discrete freezing event, the amplitude of the loss process then decreases smoothly with falling temperature. Q^{-1} values remain high at temperatures above the transition point, signifying the presence of strain coupling to some local dynamical changes, perhaps of vacancy distribution in the disordered structure. There is no strain contrast across 180° magnetic domain walls, so they cannot contribute directly to the observed variations in Q^{-1}.

5.1. Implications for palaeomagnetism

A key feature of pyrrhotite in the context of preserving palaeo-magnetic signals over long periods of geological time is that the ferrimagnetism is coupled with Fe/vacancy ordering. The coercivity of the $C2'/c'$ structure might be weak but the orientation of the net moment is likely to return to its original orientation in a crystal even after the application of a large external field because the underlying pattern of vacancy ordering will remain fixed unless the temperature is raised sufficiently to allow Fe/vacancy diffusion to occur. In other words, the orientation of a remanent signal is fixed by the underlying pattern of ferroelastic domains. However, although this should give long term stability, it raises the question of what initial signal is recorded. In the limiting case, some arbitrary configuration of domains with Fe/vacancy order could determine the net magnetisation independently of the magnetic field in which the crystal grew. To address this issue it will be necessary to develop a formal model of the $P6_3/mmc$–$C2'/c'$ transition, to include the form and strength of coupling between q_v and q_m, together with the kinetics of vacancy ordering.

6. Conclusions

Analysis of the hexagonal–monoclinic transition in a natural sample of pyrrhotite with composition close to Fe_7S_8 from the perspectives of strain and elasticity has shown:

 (a) There is significant coupling of strains with the order parameters for vacancy ordering and magnetic ordering. Monoclinic lattice geometry occurs because of strong coupling between the order parameter for vacancy ordering and the shear strain e_4. By itself, magnetoelastic coupling would cause only small deviations from hexagonal geometry.

 (b) Magnetic ordering appears to have the same continuous temperature dependence as in FeS, and the strength of coupling with strain also appears to be the same. First order character for the transition is due to the vacancy ordering. An additional and unusual coupling term, $\lambda q_m^2 q_v^8$ has emerged from considerations of symmetry and perhaps has a role in determining that magnetic ordering and vacancy ordering occur simultaneously but, individually, have markedly different trajectories with changing temperature.

 (c) Although the transition is, in principle, ferroelastic, the dynamical response to applied stress depends on the relatively long time scales required for Fe/vacancy diffusion in comparison with spin reorientation. As a consequence, changes in elastic and anelastic properties measured at RUS frequencies involve stiffening rather than softening and a pattern of acoustic loss which differs from the classical Debye freezing of ferroelastic twin walls seen in perovskites.

ORCID iDs

C R S Haines ⬤ https://orcid.org/0000-0002-1274-8329
M A Carpenter ⬤ https://orcid.org/0000-0003-2855-0007

References

[1] Andresen A F, Torbo P, Ostlund E, Bloom G and Hagen G 1967 Phase transitions in Fe$_x$S (x = 0.90-1.00) studied by neutron diffraction *Acta Chem. Scand.* **21** 2841–8
[2] Schwarz E J and Vaughan D J 1972 Magnetic phase relations of pyrrhotite *J. Geomagn. Geoelectr.* **24** 441–58
[3] Bennett C E G and Graham J 1980 New observations on natural pyrrhotites. Part III Thermomagnetic experiments *Am. Mineral.* **65** 800
[4] Grønvold F and Stølen S 1992 Thermodynamics of iron sulfides II. Heat capacity and thermodynamic properties of FeS and of Fe$_{0.875}$S at temperatures from 298.15 K to 1000 K, of Fe$_{0.98}$S from 298.15 K to 800 K, and of Fe$_{0.89}$S from 298.15 K to about 650 K *J. Chem. Thermodyn.* **24** 913–36
[5] Wang H and Salveson I 2005 A review on the mineral chemistry of the non-stoichiometric iron sulphide, Fe$_{1-x}$S ($0 \leqslant$ x $\leqslant 0.125$): polymorphs, phase relations and transitions, electronic and magnetic structures *Phase Transit.* **78** 547–67
[6] Pearce C I, Pattrick R and Vaughan D J 2006 Electrical and Magnetic Properties of Sulfides *Rev. Mineral. Geochem.* **61** 127–80
[7] Rochette P, Fillion G, Mattéi J L and Dekkers M J 1990 Magnetic transition at 30-34 Kelvin in pyrrhotite: insight into a widespread occurrence of this mineral in rocks *Earth Planet. Sci. Lett.* **98** 319–28
[8] Rochette P, Gattacceca J, Chevrier V, Hoffmann V, Lorand J-P, Funaki M and Hochleitner R 2005 Matching Martian crustal magnetization and magnetic properties of Martian meteorites *Meteorit. Planet. Sci.* **40** 529–40
[9] Rochette P, Lorand J-P, Fillion G and Sautter V 2001 Pyrrhotite and the remanent magnetization of SNC meteorites: a changing perspective on Martian magnetism *Earth Planet. Sci. Lett.* **190** 1–12
[10] Schwarz E J 1975 *Magnetic Properties of Pyrrhotite and Their Use in Applied Geology and Geophysics* (Ottawa: Dept. of Energy, Mines and Resources)
[11] Takayama T and Takagi H 2006 Phase-change magnetic memory effect in cation-deficient iron sulfide Fe$_{1-x}$S *Appl. Phys. Lett.* **88** 12512
[12] Horng C and Roberts A P 2018 The low-temperature Besnus magnetic transition: signals due to monoclinic and hexagonal pyrrhotite *Geochem., Geophys., Geosyst.* **19** 3364–75
[13] Schiemer J, Spalek L J, Saxena S S, Panagopoulos C, Katsufuji T, Bussmann-Holder A, Köhler J and Carpenter M A 2016 Magnetic field and *in situ* stress dependence of elastic behavior in EuTiO$_3$ from resonant ultrasound spectroscopy *Phys. Rev.* B **93** 54108
[14] Schiemer J A *et al* 2016 Elastic and anelastic relaxation behaviour of perovskite multiferroics I: PbZr$_{0.53}$Ti$_{0.47}$O$_3$ (PZT)–PbFe$_{0.5}$Nb$_{0.5}$O$_3$ (PFN) *J. Mater. Sci.* **51** 10727–60

[15] Schiemer J A *et al* 2017 Elastic and anelastic relaxation behaviour of perovskite multiferroics II: PbZr$_{0.53}$Ti$_{0.47}$O$_3$ (PZT)–PbFe$_{0.5}$Nb$_{0.5}$O$_3$ (PFN) *J. Mater. Sci.* **52** 285–304

[16] Evans D M, Schiemer J A, Wolf T, Adelmann P, Böhmer A E, Meingast C, Dutton S E, Mukherjee P, Hsu Y-T and Carpenter M A 2019 Strain relaxation behaviour of vortices in a multiferroic superconductor *J. Phys.: Condens. Matter* **31** 135403

[17] Carpenter M A, Evans D M, Schiemer J A, Wolf T, Adelmann P, Böhmer A E, Meingast C, Dutton S E, Mukherjee P and Howard C J 2019 Ferroelasticity, anelasticity and magnetoelastic relaxation in Co-doped iron pnictide: Ba(Fe$_{0.957}$Co$_{0.043}$)$_2$As$_2$ *J. Phys.: Condens. Matter* **31** 155401

[18] Herbert F W, Krishnamoorthy A, Yildiz B and Van Vliet K J 2015 Diffusion-limited kinetics of the antiferromagnetic to ferrimagnetic λ -transition in Fe$_{1-x}$S *Appl. Phys. Lett.* **106** 2–7

[19] Haines C R S, Howard C J, Harrison R J and Carpenter M A 2019 Group-theoretical analysis of structural instability, vacancy ordering and magnetic transitions in the system troilite (FeS) - pyrrhotite (Fe$_{1-x}$S) *Acta Crystallogr.* B **75** 1208–24

[20] Haines C R S, Dutton S E, Volk M W R and Carpenter M A 2020 Magnetoelastic properties and behaviour of 4C pyrrhotite, Fe$_7$S$_8$, through the Besnus transition *J. Phys.: Condens. Matter* **32** 405401

[21] Wolfers P, Fillion G, Ouladdiaf B, Ballou R and Rochette P 2011 The pyrrhotite 32 K magnetic transition *Solid State Phenom.* **170** 174–9

[22] Stokes H T, Hatch D M and Campbell B J *ISOTROPY Software Suite iso.byu.edu*

[23] Powell A V, Vaqueiro P, Knight K S, Chapon L C and Sanchez R D 2004 Structure and magnetism in synthetic pyrrhotite Fe$_7$S$_8$: A powder neutron-diffraction study *Phys. Rev.* B **70** 014415

[24] Carpenter M A and Salje E K H 1998 Elastic anomalies in minerals due to structural phase transitions *Eur. J. Mineral.* **10** 693–812

[25] Tenailleau C, Etschmann B, Wang H, Pring A, Grguric B A and Studer A 2005 Thermal expansion of troilite and pyrrhotite determined by *in situ* cooling (873 to 373 K) neutron powder diffraction measurements *Mineral. Mag.* **69** 205–16

[26] Salje E K H, Wruck B and Thomas H 1991 Order-parameter saturation and low-temperature extension of Landau theory *Z. Phys.* B **82** 399–404

[27] Meyer H-W, Carpenter M A, Graeme-Barber A, Sondergeld P and Schranz W 2000 Local and macroscopic order parameter variations associated with low temperature phase transitions in lawsonite, CaAl$_2$Si$_2$O$_7$(OH)$_2$·H$_2$O *Eur. J. Mineral.* **12** 1139–50

[28] Meyer H-W, Marion S, Sondergeld P, Carpenter M A, Knight K S, Redfern S A T and Dove M T 2001 Displacive components of the low-temperature phase transitions in lawsonite *Am. Mineral.* **86** 566–77

[29] Sondergeld P, Schranz W, Kityk A V, Carpenter M A and Libowitzky E 2000 Ordering behaviour of the mineral lawsonite *Phase Transit.* **71** 189–203

[30] Carpenter M A, Meyer H-W, Sondergeld P, Marion S and Knight K S 2003 Spontaneous strain variations through the low temperature phase transitions of deuterated lawsonite *Am. Mineral.* **88** 534–46

[31] Andresen A F, Hofman-Bang N, Bak T A, Varde E and Westin G 1960 Magnetic phase transitions in stoichiometric FeS studied by means of neutron diffraction *Acta Chem. Scand.* **14** 919–26

[32] Dunlop D J 2015 Transition warming and cooling remanences in pyrrhotite and hematite *Geophys. J. Int.* **203** 605–13

[33] Coelho A A 2018 TOPAS and TOPAS-Academic: an optimization program integrating computer algebra and crystallographic objects written in C++: An *J. Appl. Crystallogr.* **51** 210–8

[34] Liles D C and De Villiers J P R 2012 Redetermination of the structure of 5C pyrrhotite at low temperature and at room temperature *Am. Mineral.* **97** 257–61

[35] Allmann R and Hinek R 2007 The introduction of structure types into the Inorganic Crystal Structure Database ICSD *Acta Crystallogr.* A **63** 412–7

[36] Cheary R W, Coelho A A and Cline J P 2004 Fundamental parameters line profile fitting in laboratory diffractometers *J. Res. Natl Inst. Stand. Technol.* **109** 1–25

[37] Ben Salem M, Yangui B and Boulesteix C 1987 Abnormal orientation variants and interfaces in ferroelastics and precautions to be taken for the use of group theory (example : rare earth sesquioxides) *J. Phys.* **48** 1147–53

[38] Harries D, Pollok K and Langenhorst F 2011 Translation interface modulation in NC-pyrrhotites: Direct imaging by TEM and a model toward understanding partially disordered structural states *Am. Mineral.* **96** 716–31

[39] Bachmann F, Hielscher R and Schaeben H 2010 Texture analysis with MTEX- Free and open source software toolbox *Solid State Phenom.* **160** 63–8

[40] Tan B T, Popel A J, Wilbraham R J, Day J, Lampronti G I, Boxall C and Farnan I 2019 Surface and electrochemical controls on UO$_2$ dissolution under anoxic conditions *J. Nucl. Mater.* **520** 41–55

[41] Bitter F 1931 On Inhomogeneities in the magnetization of ferromagnetic materials *Phys. Rev.* **38** 1903–5

[42] Soffel H C 1977 Pseudo-single-domain effects and single-domain multidomain transition in natural pyrrhotite deduced from domain-structure observations *J. Geophys.* **42** 351–9

[43] Soffel H C 1981 Domain structure of natural fine-grained pyrrhotite in a rock matrix (diabase) *Phys. Earth Planet. Inter.* **26** 98–106

[44] Halgedahl S L and Fuller M 1983 The dependence of magnetic domain structure upon magnetization state with emphasis upon nucleation as a mechanism for pseudo-single-domain behavior *J. Geophys. Res. Solid Earth* **88** 6505–22

[45] Appel E, Hoffmann V and Soffel H C 1990 Magneto-optical Kerr effect in (titano)magnetite, pyrrhotite and hematite *Phys. Earth Planet. Inter.* **65** 36–42

[46] O'Reilly W, Hoffmann V, Chouker A C, Soffel H C and Menyeh A 2000 Magnetic properties of synthetic analogues of pyrrhotite ore in the grain size range 1-24 μm *Geophys. J. Int.* **142** 669–83

[47] Li G and Gladden J R 2011 High temperature resonant ultrasound spectroscopy: a review *Int. J. Spectrosc.* **2010** 206362

[48] Migliori A, Sarrao J L, Visscher W M, Bell T M, Lei M, Fisk Z and Leisure R G 1993 Resonant ultrasound spectroscopic techniques for measurement of the elastic moduli of solids *Phys. B Condens. Matter* **183** 1–24

[49] Zadler B J, Le Rousseau J H L, Scales J A and Smith M L 2004 Resonant ultrasound spectroscopy: theory and application *Geophys. J. Int.* **156** 154–69

[50] Maynard J 1996 Resonant ultrasound spectroscopy *Phys. Today* **49** 26

[51] Migliori A and Maynard J D 2005 Implementation of a modern resonant ultrasound spectroscopy system for the measurement of the elastic moduli of small solid specimens *Rev. Sci. Instrum.* **76** 121301

[52] Li F and Franzen H F 1996 Phase transitions in near stoichiometric iron sulfide *J. Alloys Compd.* **238** 73–80

[53] Grønvold F and Stølen S 1992 Thermodynamics of iron sulfides II. Heat capacity and thermodynamic properties of FeS and of Fe$_{0.875}$S at temperatures from 298.15 K to 1000 K, of Fe$_{0.98}$S from 298.15 K to 800 K, and of Fe0.89S from 298.15 K to about 650 K *J. Chem. Thermodyn.* **24** 913–36

[54] Salje E and Devarajan V 1986 Phase transitions in systems with strain-induced coupling between two order parameters *Phase Transit.* **6** 235–47

[55] Bennett C E G and Graham J 1981 New observations on natural pyrrhotites: magnetic transition in hexagonal pyrrhotite *Am. Mineral.* **66** 1254–7

[56] Marusak L A and Mulay L N 1980 Polytypism in the cation-deficient iron sulfide, Fe_9S_{10}, and the magnetokinetics of the diffusion process at temperatures about the antiferro- to ferrimagnetic (λ) phase transition *Phys. Rev.* B **21** 238–44

[57] Salje E K H and Carpenter M A 2011 Linear–quadratic order parameter coupling and multiferroic phase transitions *J. Phys.: Condens. Matter* **23** 462202

[58] Rehwald W 1973 The study of structural phase transitions by means of ultrasonic experiments *Adv. Phys.* **22** 721–55

[59] Lüthi B and Rehwald W 1981 Ultrasonic studies near structural phase transitions *Structural Phase Transitions I* ed K A Müller and H Thomas (Berlin: Springer) pp 131–84

[60] Thomson R I, Chatterji T and Carpenter M A 2014 CoF_2: a model system for magnetoelastic coupling and elastic softening mechanisms associated with paramagnetic $\leftrightarrow$ antiferromagnetic phase transitions *J. Phys.: Condens. Matter* **26** 146001

[61] Carpenter M A 2015 Static and dynamic strain coupling behaviour of ferroic and multiferroic perovskites from resonant ultrasound spectroscopy *J. Phys.: Condens. Matter* **27** 263201